Petroleum Science 21 (2024) 1597–1610

Contents lists available at ScienceDirect

Petroleum Science

journal homepage: www.keaipublishing.com/en/journals/petroleum-science

Original Paper

Helmholtz decomposition with a scalar Poisson equation in elastic anisotropic media

Xin-Yu Fang [a, b], Gang Yao [a, b, *], Qing-Qing Zheng [a, c], Ping-Min Zhang [a, b], Di Wu [a, d], Feng-Lin Niu [e]

[a] State Key Laboratory of Petroleum Resources and Engineering, China University of Petroleum (Beijing), Beijing, 102249, China
[b] Unconventional Petroleum Research Institute, China University of Petroleum (Beijing), Beijing, 102249, China
[c] Department of Mathematics, College of Science, China University of Petroleum (Beijing), Beijing, 102249, China
[d] College of Geophysics, China University of Petroleum (Beijing), Beijing, 102249, China
[e] Department of Earth, Environmental and Planetary Sciences, Rice University, Houston, TX, 77005, USA

ARTICLE INFO

Article history:
Received 1 July 2023
Received in revised form
23 September 2023
Accepted 6 December 2023
Available online 12 December 2023

Edited by Jie Hao and Meng-Jiao Zhou

Keywords:
Anisotropic media
Scalar anisotropic Poisson equation
Improved elastic wavefield decomposition

ABSTRACT

P- and S-wave separation plays an important role in elastic reverse-time migration. It can reduce the artifacts caused by crosstalk between different modes and improve image quality. In addition, P- and S-wave separation can also be used to better understand and distinguish wave types in complex media. At present, the methods for separating wave modes in anisotropic media mainly include spatial non-stationary filtering, low-rank approximation, and vector Poisson equation. Most of these methods require multiple Fourier transforms or the calculation of large matrices, which require high computational costs for problems with large scale. In this paper, an efficient method is proposed to separate the wave mode for anisotropic media by using a scalar anisotropic Poisson operator in the spatial domain. For 2D problems, the computational complexity required by this method is 1/2 of the methods based on solving a vector Poisson equation. Therefore, compared with existing methods based on pseudo-Helmholtz decomposition operators, this method can significantly reduce the computational cost. Numerical examples also show that the P and S waves decomposed by this method not only have the correct amplitude and phase relative to the input wavefield but also can reduce the computational complexity significantly.

1. Introduction

The P- and S-waves are coupled during their propagation in the Earth. Thus, crosstalk artifacts will occur when imaging directly with the mixed wavefields, affecting the imaging quality (Zhang and Shi, 2019; Xie et al., 2021). Through wave-mode separation, the PP, PS, SS and SP waves can be imaged separately, which can reduce wave-mode crosstalk artifacts and improve imaging quality (Sun et al., 2006; Yan and Sava, 2008; Zhou et al., 2019; Yang et al., 2019; Li et al., 2021; Li and Qu, 2022; Zhang et al., 2022; Zuo et al., 2022). The application of wave mode separation in full-waveform inversion can reduce the nonlinearity and crosstalk problem between multi-parameters and improve the accuracy of inversion (Ren and Liu, 2016; Qu et al., 2018; Luo et al., 2020; Hu et al., 2022). So P- and S-wave separation is very important in imaging and full-waveform inversion for elastic isotropic and anisotropic media.

The key to wavefield separation is the polarization directions of the P and S waves. In isotropic media, the wave travels in the same direction as the polarization of the P-wave and perpendicular to the polarization of the S-wave, so the P and S waves can be separated by applying divergence and curl directly to the input wavefield. However, the resulting amplitude and phase of the P and S waves are incorrect (Sun et al., 2004). Separating the input wavefield using Helmholtz decomposition (Morse and Feshbach, 1953; Aki and Richards, 2002) can solve this problem effectively. However, directly solving scalar and vector potentials requires calculating triple integrals, resulting in high costs. To solve this problem, the Helmholtz decomposition based methods for vector decomposing wavefield in the space domain and the wavenumber domain are proposed successively (Zhang and McMechan, 2010; Zhu, 2017). Yang et al. (2018) and Zhao et al. (2018) propose to integrate the source wavelet and achieve the wavefield decomposition by scaling

* Corresponding author.
E-mail address: yaogang@cup.edu.cn (G. Yao).

https://doi.org/10.1016/j.petsci.2023.12.007

the decomposition operator. This method avoids the calculation of Poisson equation and improves the efficiency of wavefield decomposition. Using the relationship between the divergence, curl, gradient, and exterior derivative operations (Morse and Feshbach, 1953), Zheng and Yao (2023) proposed a method for decomposing wavefields in isotropic media based on a scalar Laplacian operator. Different from the existing Helmholtz decomposition based method, this method only requires solving a scalar Poisson equation, not a vector Poisson equation, resulting in much higher computational efficiency.

In anisotropic media, the polarization directions of P and S waves are neither parallel nor perpendicular to the wave propagation direction. Therefore, it is necessary to obtain the polarization directions of P and S waves through the Christoffel equation (Dellinger and Etgen, 1990), and then project the vector of wave displacement or particle velocity into the polarization directions of P and S waves to achieve wave mode separation. Dellinger and Etgen (1990) and Dellinger (1991) obtained the polarization directions of P and S waves by solving the Christoffel equation in the wavenumber domain and then returned to the spatial domain to obtain the anisotropic wavefield separation operator. However, since this method directly applies the separation operator to the wavefield, the amplitude and the phase obtained are incorrect. Moreover, this method is only accurate for homogeneous media. To solve these problems, Zhang and McMechan (2010) proposed a vector decomposition method of elastic wavefield in the wavenumber domain, which can obtain the correct amplitude and phase. Yan and Sava (2009) proposed a non-stationary filter to separate P- and S-wave in anisotropic heterogeneous media. Their method needs to solve the Christoffel equation of local media parameters to obtain the local polarization direction for constructing the non-stationary filter, which leads to high computational costs. To reduce computational costs, many scholars have proposed other approaches, such as low-rank approximation (Cheng and Fomel, 2014; Sripanich et al., 2017), LU decomposition (Yang et al., 2019), ani-Helmholtz decomposition in the wavenumber domain and the spatial domain (Zhang et al., 2022, 2023). In addition, Zhou and Wang (2017) used the Poynting vector to estimate the deviation angle between the vector of wave displacement and the P-wave polarization direction and then separated the P and S waves by rotating the wave vector to the P-wave polarization direction. Lu et al. (2019) used the Poynting vector to achieve wave-mode separation in the angle domain.

In this paper, we extend the method proposed by Zheng and Yao (2023) to separate the anisotropic elastic wavefields by using the pseudo-gradient operator (Zuo et al., 2022). For the resulting method, we only need to solve an scalar anisotropic Poisson equation. Compared with the methods that require solving vector anisotropic Poisson equations, our method can greatly reduce the computational cost. Precisely, in the case of 2D wavefields, our method can save half of the computational cost. Like the methods proposed by Du et al. (2017) and Zhong et al. (2021), we obtain the S-wave by subtracting the vector P-wave directly from the input full wavefield. There is no curl operation on a certain auxiliary wavefield, which can further reduce the computation costs when compared with existing pseudo-Helmholtz decomposition methods.

2. Method

2.1. Review of the pseudo-Helmholtz decomposition operator for 2D VTI media

The elastic wave equation in the 2D VTI media is as follows:

$$\begin{cases} \rho(\mathbf{x})\dfrac{\partial^2 u_x(\mathbf{x},t)}{\partial t^2} = c_{11}(\mathbf{x})\dfrac{\partial^2 u_x(\mathbf{x},t)}{\partial x^2} + c_{55}(\mathbf{x})\dfrac{\partial^2 u_x(\mathbf{x},t)}{\partial z^2} + (c_{13}(\mathbf{x}) + c_{55}(\mathbf{x}))\dfrac{\partial^2 u_z(\mathbf{x},t)}{\partial x \partial z} \\ \rho(\mathbf{x})\dfrac{\partial^2 u_z(\mathbf{x},t)}{\partial t^2} = c_{55}(\mathbf{x})\dfrac{\partial^2 u_z(\mathbf{x},t)}{\partial x^2} + c_{33}(\mathbf{x})\dfrac{\partial^2 u_z(\mathbf{x},t)}{\partial z^2} + (c_{13}(\mathbf{x}) + c_{55}(\mathbf{x}))\dfrac{\partial^2 u_x(\mathbf{x},t)}{\partial x \partial z} \end{cases} \tag{1}$$

where $\mathbf{x}$ is spatial position coordinates, $u_x(\mathbf{x},t)$ and $u_z(\mathbf{x},t)$ denote horizontal and vertical components of the displacement or particle velocity wavefields, respectively. $\rho(\mathbf{x})$ represents density, and $c_{11}(\mathbf{x})$, $c_{13}(\mathbf{x})$, $c_{33}(\mathbf{x})$, $c_{55}(\mathbf{x})$ are the elements of the elastic coefficient matrix.

Taking the Fourier transform of Eq. (1) by assuming the local homogenous medium, the Christoffel equation is obtained:

$$\rho\omega^2 \begin{bmatrix} U_x \\ U_z \end{bmatrix} = \begin{bmatrix} c_{11}k_x^2 + c_{55}k_z^2 & (c_{13}+c_{55})k_x k_z \\ (c_{13}+c_{55})k_x k_z & c_{55}k_x^2 + c_{33}k_z^2 \end{bmatrix} \begin{bmatrix} U_x \\ U_z \end{bmatrix} \tag{2}$$

where ω is the angular frequency, U_x and U_z are the corresponding wavefields of u_x and u_z after the Fourier transform, respectively. Moreover, k_x and k_z are the wavenumbers in the x and z directions, respectively. Denoting

$$\mathbf{A} = \begin{bmatrix} c_{11}k_x^2 + c_{55}k_z^2 & (c_{13}+c_{55})k_x k_z \\ (c_{13}+c_{55})k_x k_z & c_{55}k_x^2 + c_{33}k_z^2 \end{bmatrix} \text{ and } \tilde{\mathbf{a}} = \begin{bmatrix} U_x \\ U_z \end{bmatrix} \tag{3}$$

Then $\lambda = \rho\omega^2 = \rho k^2 V^2$, where V is the phase velocity, λ and $\tilde{\mathbf{a}}$ are the eigenvalue and eigenvector of matrix $\mathbf{A}$, respectively. The matrix $\mathbf{A}$ has two eigenvalues, and the eigenvectors corresponding to the large and small eigenvalues are the polarization directions of the P and S waves, respectively. Moreover, the elastic coefficient matrix elements in Eq. (3) can be represented by Thomsen parameters (Thomsen, 1986) as follows:

$$\begin{aligned} &c_{11} = \rho(1+2\varepsilon)v_p^2, c_{33} = \rho v_p^2, c_{55} = \rho v_s^2 \\ &c_{13} = \rho\sqrt{\left[(1+2\delta)v_p^2 - v_s^2\right]\left[v_p^2 - v_s^2\right]} - \rho v_s^2 \end{aligned} \tag{4}$$

where ε and δ are the Thomsen anisotropy parameters, v_p and v_s denote the P and S velocities along the axis of symmetry, respectively. Therefore, the eigenvalue of matrix $\mathbf{A}$ is

$$\lambda_{1,2}=\rho\frac{\left[(1+2\varepsilon)v_{\mathrm{p}}^2+v_{\mathrm{s}}^2\right]k_x^2+\left[v_{\mathrm{p}}^2+v_{\mathrm{s}}^2\right]k_z^2}{2}\pm\rho\frac{\left[(1+2\varepsilon)v_{\mathrm{p}}^2-v_{\mathrm{s}}^2\right]k_x^2+\left[v_{\mathrm{p}}^2-v_{\mathrm{s}}^2\right]k_z^2}{2}\times\sqrt{1+\frac{8(\delta-\varepsilon)v_{\mathrm{p}}^2\left(v_{\mathrm{p}}^2-v_{\mathrm{s}}^2\right)k_x^2k_z^2}{\left[\left((1+2\varepsilon)v_{\mathrm{p}}^2-v_{\mathrm{s}}^2\right)k_x^2+\left(v_{\mathrm{p}}^2-v_{\mathrm{s}}^2\right)k_z^2\right]^2}}\tag{5}$$

Utilizing the zero-order Taylor expansion (Zuo et al., 2022), the eigenvalues and eigenvectors of **A** can be approximately expressed as

$$\lambda_1=\rho v_{\mathrm{p}}^2\left[(1+2\varepsilon)k_x^2+k_z^2\right],\ \lambda_2=\rho v_{\mathrm{s}}^2\left[k_x^2+k_z^2\right]$$
$$\tilde{\mathbf{a}}_1=\begin{bmatrix}k_x\\ \dfrac{\sqrt{\left[(1+2\delta)v_{\mathrm{p}}^2-v_{\mathrm{s}}^2\right]\left[v_{\mathrm{p}}^2-v_{\mathrm{s}}^2\right]}}{(1+2\varepsilon)v_{\mathrm{p}}^2-v_{\mathrm{s}}^2}k_z\end{bmatrix}$$
$$\tilde{\mathbf{a}}_2=\begin{bmatrix}\dfrac{\sqrt{\left[(1+2\delta)v_{\mathrm{p}}^2-v_{\mathrm{s}}^2\right]\left[v_{\mathrm{p}}^2-v_{\mathrm{s}}^2\right]}}{(1+2\varepsilon)v_{\mathrm{p}}^2-v_{\mathrm{s}}^2}k_z\\ -k_x\end{bmatrix}\tag{6}$$

By denoting (Zuo et al., 2022)

$$r=\frac{\sqrt{\left[(1+2\delta)v_{\mathrm{p}}^2-v_{\mathrm{s}}^2\right]\left[v_{\mathrm{p}}^2-v_{\mathrm{s}}^2\right]}}{(1+2\varepsilon)v_{\mathrm{p}}^2-v_{\mathrm{s}}^2}\tag{7}$$

the corresponding formulas of Eq. (6) in the spatial domain are

$$\mathbf{a}_1(\mathbf{x})=\begin{bmatrix}\partial_x\\ r(\mathbf{x})\partial_z\end{bmatrix}$$
$$\mathbf{a}_2(\mathbf{x})=\begin{bmatrix}r(\mathbf{x})\partial_z\\ -\partial_x\end{bmatrix}\tag{8}$$
$$r(\mathbf{x})=\frac{\sqrt{\left[(1+2\delta(\mathbf{x}))v_{\mathrm{p}}^2(\mathbf{x})-v_{\mathrm{s}}^2(\mathbf{x})\right]\left[v_{\mathrm{p}}^2(\mathbf{x})-v_{\mathrm{s}}^2(\mathbf{x})\right]}}{(1+2\varepsilon(\mathbf{x}))v_{\mathrm{p}}^2(\mathbf{x})-v_{\mathrm{s}}^2(\mathbf{x})}$$

where, ∂_x and ∂_z are the first-order spatial derivatives in x and z directions, respectively. Physically, $\mathbf{a}_1(\mathbf{x})$ and $\mathbf{a}_2(\mathbf{x})$ denote the polarization directions of the P- and S-wave, respectively. Since zero-order Taylor expansion is applied to obtain the eigenvalues and eigenvectors of **A**, the resulting eigenvalues in Eq. (6) and eigenvectors in Eq. (8) are accurate for elliptical anisotropy media, i.e., $\varepsilon=\delta$. When the difference between ε and δ is large, the accuracy of zero-order Taylor expansion decreases.

According to Eq. (8), which gives approximated eigenvectors of **A**, the following operator gives a pseudo-gradient operator in anisotropic media:

$$\overline{\nabla}=\begin{bmatrix}\partial_x\\ r(\mathbf{x})\partial_z\end{bmatrix}\tag{9}$$

Since the P- and S-wave polarization directions are perpendicular to each other, the decomposition formulas of P and S waves can be obtained from the zero-order pseudo-Helmholtz decomposition operator:

$$\mathbf{u}^{\mathrm{p}}=\overline{\nabla}(\overline{\nabla}\cdot\mathbf{w}),\ \ \mathbf{u}^{\mathrm{s}}=-\overline{\nabla}\times(\overline{\nabla}\times\mathbf{w})\tag{10}$$

The vector wavefield **w** satisfies the following anisotropic Poisson equation:

$$\frac{\partial^2\mathbf{w}(\mathbf{x})}{\partial x^2}+r^2(\mathbf{x})\frac{\partial^2\mathbf{w}(\mathbf{x})}{\partial z^2}=\mathbf{u}(\mathbf{x})\tag{11}$$

Eqs. (9)–(11) are the anisotropic wavefield decomposition formulas. When the anisotropy parameter is 0, Eq. (9) reduces to a gradient operator. Therefore, the approximate gradient operator of Eq. (9) is an improvement on the counterpart in Yang et al. (2019). Eq. (11) indicates that **w** is obtained by solving a vector Poisson equation, which contains multiple scalar Poisson equations. When the scale of **u** increases, the computational cost of solving the vector Poisson equation (Eq. (11)) will increase significantly.

2.2. A scalar anisotropic Poisson operator

By using relationships among the gradient, divergence, curl, and exterior derivative operations, Zheng and Yao (2023) proposed the method of using a scalar Poisson equation to decompose the isotropic wavefield. In this section, we extend this method to decompose anisotropic wavefields. By introducing an auxiliary function, we present a scalar anisotropic Poisson equation based on the pseudo-divergence, pseudo-gradient, and pseudo-curl operators.

For anisotropic media, the input wavefield vector can be projected to the polarization directions of P and S waves according to the Helmholtz decomposition theory. Here, the obtained spatial domain approximate P-wave polarization direction is used to replace the P-wave polarization direction. The pseudo-gradient operator given by Eq. (9) is consistent with the polarization direction of the P-wave and orthogonal to the polarization direction of the S-wave. Therefore, the following formula in the spatial domain is obtained after projecting the vector wavefields **u**, $\mathbf{u}^{\mathrm{p}}$ and $\mathbf{u}^{\mathrm{s}}$ onto the obtained polarization vectors $\mathbf{a}_1(\mathbf{x})$, $\mathbf{a}_2(\mathbf{x})$:

$$\mathbf{u}=\mathbf{u}^{\mathrm{p}}+\mathbf{u}^{\mathrm{s}}$$
$$\overline{\nabla}\cdot\mathbf{u}=\overline{\nabla}\cdot\mathbf{u}^{\mathrm{p}},\ \ \overline{\nabla}\times\mathbf{u}=\overline{\nabla}\times\mathbf{u}^{\mathrm{s}}$$
$$\overline{\nabla}\times\mathbf{u}^{\mathrm{p}}=0,\ \ \overline{\nabla}\cdot\mathbf{u}^{\mathrm{s}}=0\tag{12}$$

More details can be seen in Zhang et al. (2022). Here, **u**, $\mathbf{u}^{\mathrm{p}}$ and $\mathbf{u}^{\mathrm{s}}$ are the input vector wavefield, vector P-wave, and vector S-wave, respectively.

For the general VTI anisotropic media, the gradient and curl operators are complex. Thus, we obtain them by applying zero-order Taylor expansion to the exact eigenvalue of **A**. Applying the pseudo-gradient operator to Theorem 1 of Zheng and Yao (2023) and combining it with the properties of P and S waves in Eq. (12),

the following equation can be obtained:

$$\mathbf{u} - \mathbf{u}^{\mathrm{s}} = \overline{\nabla} f \tag{13}$$

Applying the pseudo-divergence operator to both sides of Eq. (13) results in

$$\overline{\nabla}^2 f = \overline{\nabla} \cdot (\overline{\nabla} f) = \overline{\nabla} \cdot \mathbf{u} \tag{14}$$

which can be rewritten as

$$\frac{\partial^2 f(\mathbf{x})}{\partial x^2} + r^2(\mathbf{x}) \frac{\partial^2 f(\mathbf{x})}{\partial z^2} = \overline{\nabla} \cdot \mathbf{u}(\mathbf{x}) \tag{15}$$

Therefore, the P- and S-wavefield decomposition equations for VTI anisotropic media are

$$\mathbf{u}^{\mathrm{p}} = \overline{\nabla} f, \ \mathbf{u}^{\mathrm{s}} = \mathbf{u} - \mathbf{u}^{\mathrm{p}} \tag{16}$$

From Eqs. (15) and (16), it can be seen that the computational complexity of implementing wavefield decomposition is mainly reflected in solving the scalar anisotropic Poisson Eq. (15). By contrast, the separation presented by Yang et al. (2019) needs to solve the vector anisotropic Poisson equation (e.g., Eq. (11)). For the 2D case, two anisotropic Poisson equations need to be solved. The method proposed in this paper only requires solving one Poisson equation. Theoretically, the computational cost of our proposed method is almost 1/2 of that of Yang et al. (2019) for 2D problems. An extension of this method for 3D cases can be found in Appendix A.

2.3. Numerical implementation

According to Eqs. (14)–(16), the proposed wavefield decomposition method includes four steps: (1) calculate $\overline{\nabla} \cdot \mathbf{u}$; (2) solve the scalar anisotropic Poisson equation; (3) compute $\overline{\nabla} f$ to produce the P-wave; (4) compute the S-wave by subtracting the P-wave from the full wavefield.

Usually, staggered finite-difference methods are used to solve the VTI elastic wave equations, resulting in a half-grid shift of the velocity and stress components. In the first step, we use the staggered grid finite difference to compute $\overline{\nabla} \cdot \mathbf{u}$. The obtained scalar field is located at the grid points of normal stresses. The calculation in the second step operates on the grid points of normal stresses. In the third and fourth steps, the P-wave is obtained by solving $\overline{\nabla} f$ using finite difference, and then the S-wave is obtained by subtracting the P-wave from the full wavefield. Therefore, the separated P/S waves are still in the original grid position.

In the second step, the successive over-relaxation (SOR) iterative method (Kincaid and Young, 1972) is used to solve the scalar anisotropic Poisson equation (Eq. (15)). Here, the second-order spatial derivative of the function is computed with the sixth-order central finite difference.

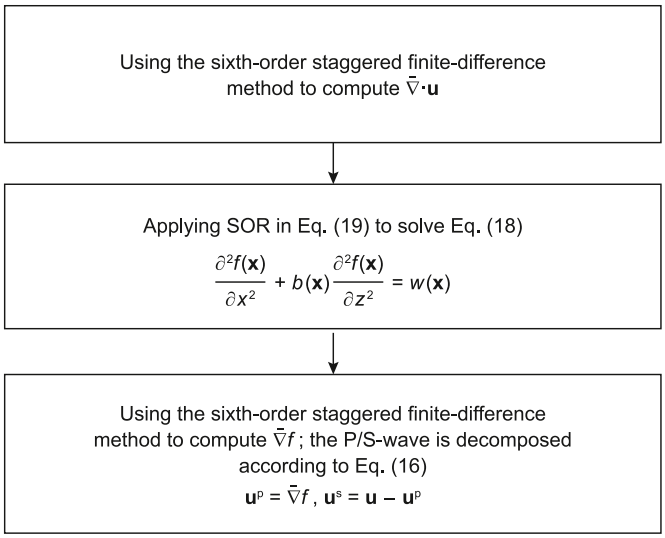

Fig. 1. Flowchart of P/S-wave decomposition.

By denoting

$$b(\mathbf{x}) = r^2(\mathbf{x}), w(\mathbf{x}) = \overline{\nabla} \cdot \mathbf{u}(\mathbf{x}) \tag{17}$$

Eq. (15) can be expressed as

$$\frac{\partial^2 f(\mathbf{x})}{\partial x^2} + b(\mathbf{x}) \frac{\partial^2 f(\mathbf{x})}{\partial z^2} = w(\mathbf{x}) \tag{18}$$

The SOR iteration format for Eq. (18) is as follows:

$$f_{i,j}^{(k+1)} = \beta \frac{w_{i,j} - \frac{1}{\Delta x^2} \sum_{n=1}^{3} c_n \left(f_{i+n,j}^{(k)} + f_{i-n,j}^{(k+1)} \right) - \frac{b_{i,j}}{\Delta z^2} \sum_{n=1}^{3} c_n \left(f_{i,j+n}^{(k)} + f_{i,j-n}^{(k+1)} \right)}{c_0 \left(\frac{1}{\Delta x^2} + \frac{b_{i,j}}{\Delta z^2} \right)} + (1-\beta) f_{i,j}^{(k)} \tag{19}$$

where $f_{i,j}^{(k)}$ represents the value of f on the grid point (i, j) of the k-th iteration, β is the relaxation factor of the SOR iterative method, and c_n is the finite-difference coefficient. The convergence condition of this iterative method is $0 < \beta < 2$. In the numerical experiments of this paper, the relaxation factor β of the SOR iterative is obtained through trial and error in the interval $[0, 2]$, which is taken as 1.9. To speed up the convergence, we adopt the SOR iteration with alternating sweeping orderings (Zhao, 2005) to solve the scalar Poisson equation. The four alternating sweeping orderings in the entire domain are as follows:

$$\begin{array}{ll} \text{(i) } i = 1{:}I,\ j = 1{:}J, & \text{(ii) } i = I{:}\ 1,\ j = 1{:}J \\ \text{(iii) } i = I{:}\ 1,\ j = J{:}\ 1, & \text{(iv) } i = 1{:}I,\ j = J{:}\ 1 \end{array} \tag{20}$$

Eq. (20) indicates the update order of Eq. (19). One iteration uses

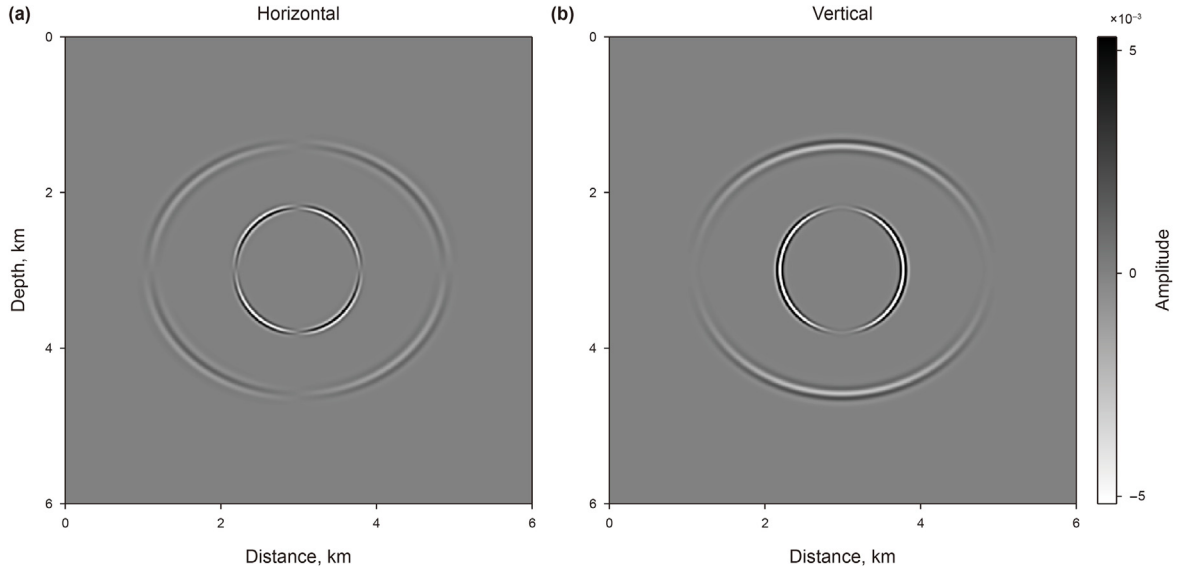

Fig. 2. The horizontal **(a)** and vertical **(b)** components of particle velocity for the elliptical anisotropic homogeneous model.

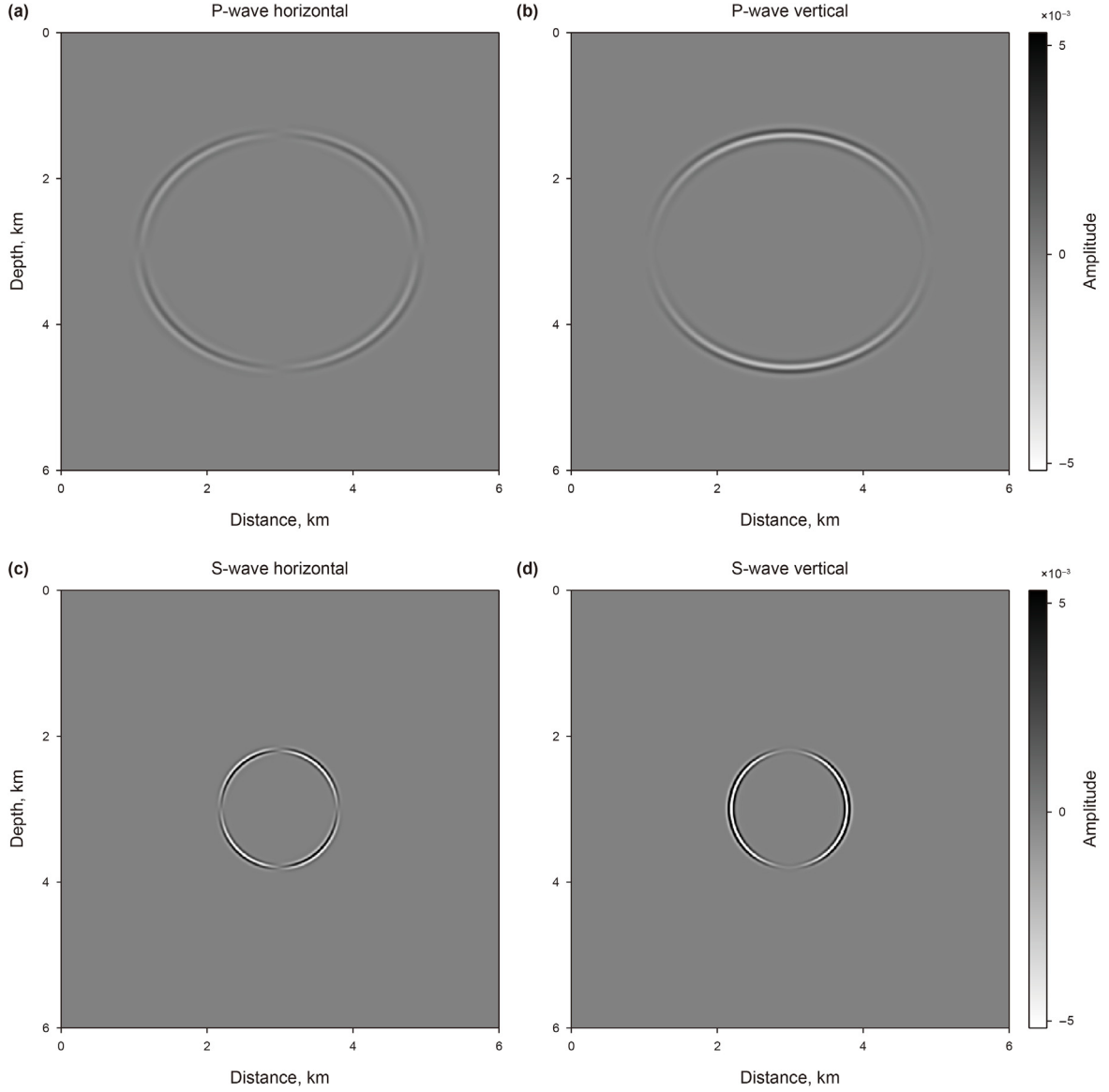

Fig. 3. The separated wavefields for the elliptical anisotropic homogeneous model. Horizontal **(a)** and vertical **(b)** components of P-wave. Horizontal **(c)** and vertical **(d)** components of *S*-wave.

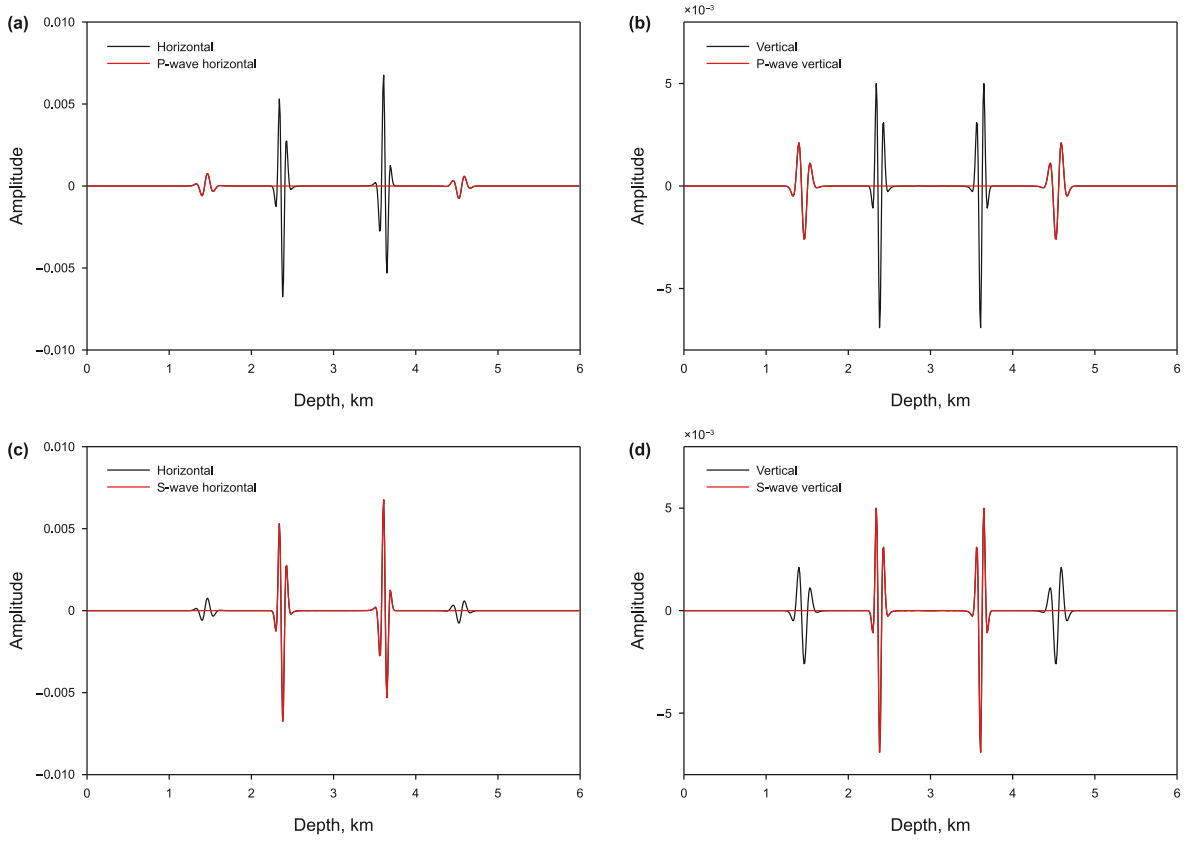

Fig. 4. The wiggle display of the 350th trace (distance = 3.5 km) for the experiment of the elliptical anisotropic homogeneous model. The black curves show the original wavefield while the red curves show the separated P/S waves.

the order of (i), and the next three iterations follows the order of (ii) – (iv), and then repeat the order of (i) and so on. The solution obtained in each iteration is used as the initial value of the next iteration. Based on the description in this section, Fig. 1 is presented to show the working flowchart.

3. Examples

In this section, four numerical examples are presented to demonstrate the effectiveness of our proposed method for decomposing the wavefields in anisotropic media.

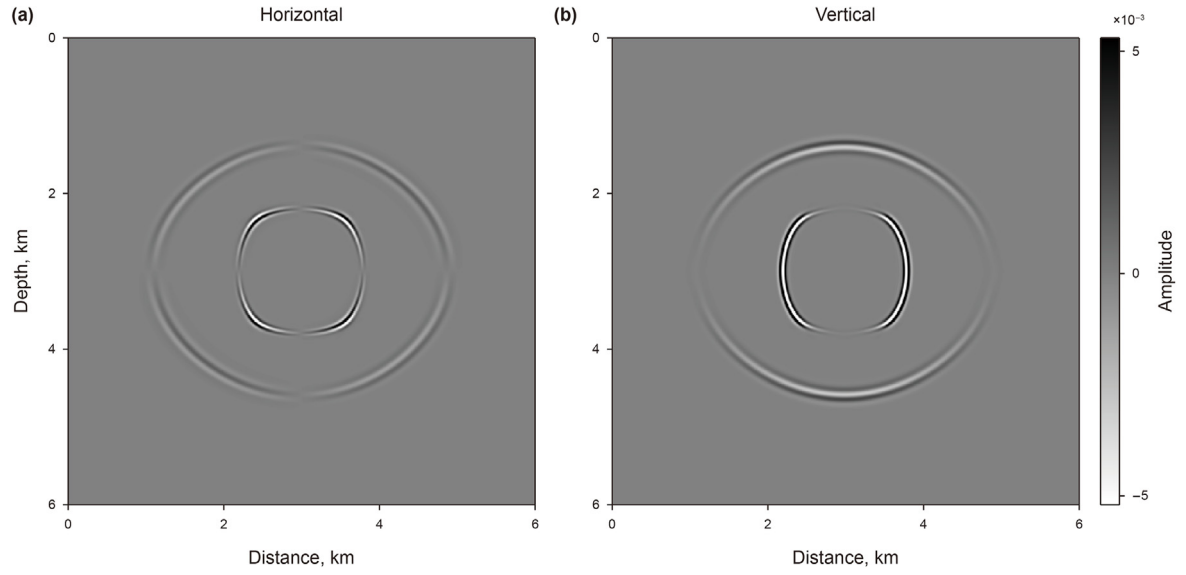

Fig. 5. The horizontal **(a)** and vertical **(b)** components of particle velocity for the non-elliptical anisotropic homogeneous model.

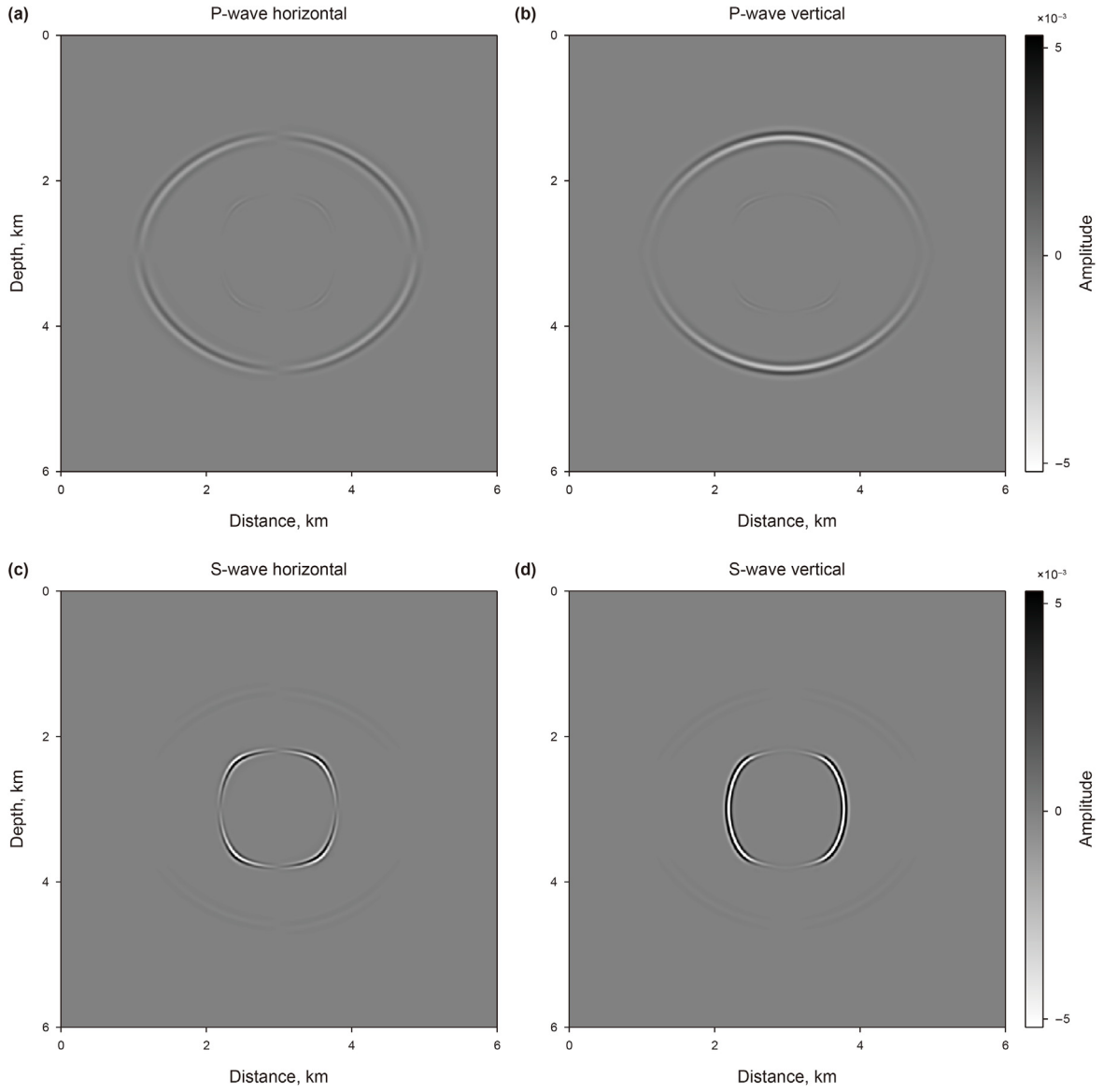

Fig. 6. The separated wavefields for the non-elliptical anisotropic homogeneous model. Horizontal **(a)** and vertical **(b)** components of P-wave. Horizontal **(c)** and vertical **(d)** components of S-wave.

3.1. Elliptical anisotropic homogeneous model

The first example is the elliptical anisotropic homogeneous model. A 15 Hz Ricker wavelet is used as the vertical body-force source excitation, and the source location is at the center of the model. The parameters of the model are $v_p = 3000$ m/s, $v_s = 1500$ m/s, $\rho = 1000$ kg/m^3, $\varepsilon = 0.2$ and $\delta = 0.2$. Moreover, the model is discretized into a grid of 600 $\times$ 600 with a 10 m grid interval.

The horizontal and vertical particle velocity wavefields are shown in Fig. 2. Fig. 3 shows the horizontal and vertical components of P and S waves obtained by using the decomposition method proposed in this paper, i.e., Eqs. (14)–(16). As can be seen from Fig. 3, P- and S-wavefield can be separated completely for an elliptical anisotropic model. The wiggle comparison of the 350th trace is shown in Fig. 4. It can be seen from Fig. 4 that the horizontal and vertical components of P and S waves obtained by the proposed method match well with the amplitude and phase of the input velocity wavefields. This further demonstrates the effectiveness of the proposed method.

3.2. Non-elliptical anisotropic homogeneous model

In this experiment, we test the performance of the proposed zero-order method for a non-elliptical anisotropic homogeneous media. The test parameters are the same as that of the previous elliptical anisotropic model except for $\delta = 0.1$. The horizontal and vertical particle velocity wavefields are shown in Fig. 5. Fig. 6 shows the horizontal and vertical components of P and S waves.

It can be seen from Fig. 6 that there is a small amount of S-wave leaking into the separated P-wave, and there is also some P-wave residual in the S-wave. Furthermore, according to the wiggle display in Fig. 7, the residual is about 3% in terms of the amplitude ratio. This is because the polarization directions of the P and S waves shown in Eq. (8) are exact in elliptical anisotropic media but are an approximation in non-elliptical anisotropic media, so there will be some residuals when decomposing non-elliptical anisotropic wavefield. The amplitude of the residual is

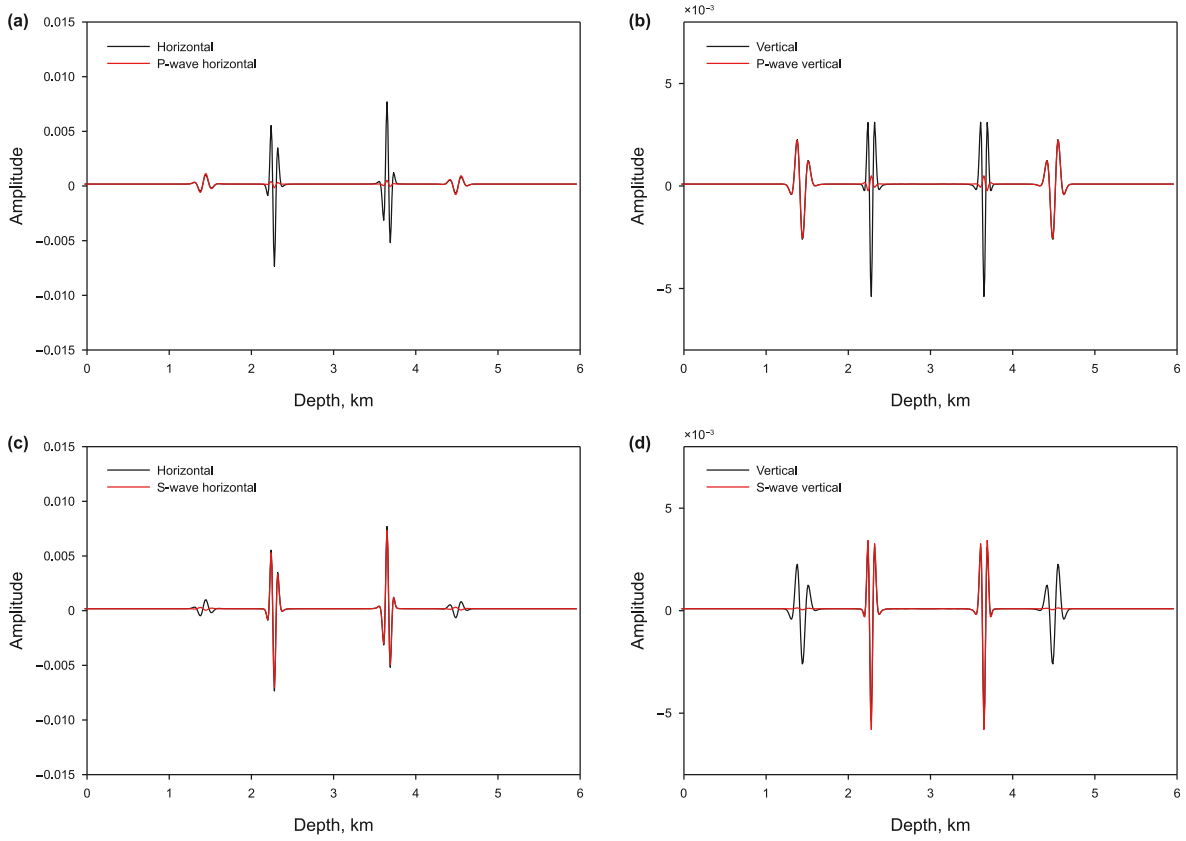

Fig. 7. The wiggle display of the 350th trace (distance = 3.5 km) for the experiment of the non-elliptical anisotropic homogeneous model. The black curves show the original wavefield while the red curves show the separated P/S waves.

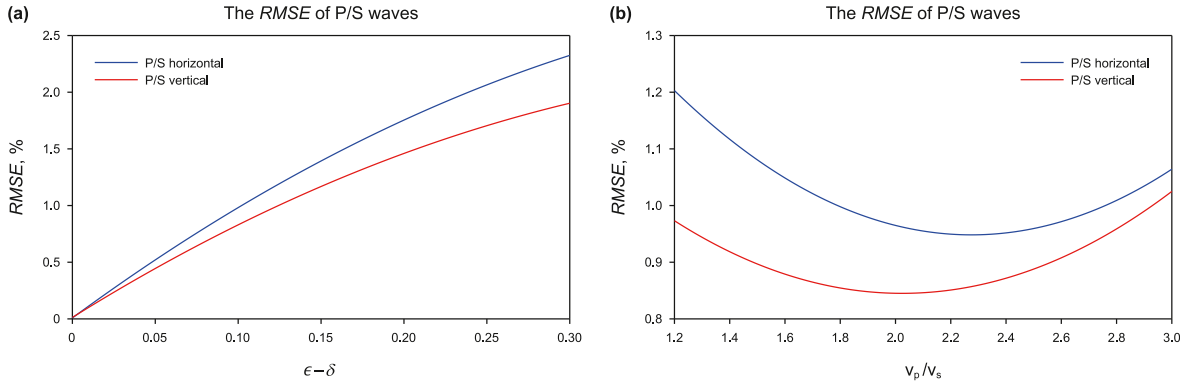

Fig. 8. Root mean square errors (*RMSE*) of the P/S waves obtained by using the proposed method relative to the accurate P/S waves with different influential factors: **(a)** anisotropic parameter difference, i.e., $\varepsilon - \delta$ and **(b)** the ratio of P-wave to S-wave velocities, i.e., v_p/v_s.

proportional to the difference between ε and δ. Although the leakage exists, previous studies (Yang et al., 2019; Zhang et al., 2022; Zuo et al., 2022) suggest that the zero-order pseudo-Helmholtz decomposition method fulfills the quality requirement of elastic migration.

Because accurate P/S wavefileds can be obtained by cutting through a homogeneous model, we take homogeneous non-elliptical media as an example to further analyze the accuracy of this method. By keeping other parameters fixed, we separately change the anisotropic parameter difference, i.e., $\varepsilon - \delta$ and the ratio of P-wave to S-wave velocities, i.e., v_p/v_s. We then calculate the root mean square error (*RMSE*) of the P/S waves obtained by using the method proposed in this paper relative to the accurate P/S waves. The results are shown in Fig. 8.

When $v_p/v_s = \sqrt{3}, v_p = 3000\,\mathrm{m/s}, v_s = 1732\mathrm{m/s}, \rho = 1000\,\mathrm{kg/m^3}, \delta = 0.1$ and the range of $\varepsilon - \delta$ is [0, 0.3], the *RMSE* of P/S waves obtained using the proposed approach are shown in Fig. 8(a). As can be seen, when other parameters are fixed, the *RMSE* is directly proportional to $\varepsilon - \delta$. Furthermore, the *RMSE* of the vertical component is smaller than that of the horizontal component.

When $v_p = 3000$ m/s, $\rho = 1000\,\mathrm{kg/m^3}$, $\varepsilon = 0.2$, $\delta = 0.1$, the *RMSE* relative to v_p/v_s is shown in Fig. 8(b). As can be seen, when v_p/v_s is between 1.2 and 3, the *RMSE* is less than 1.2 %. The horizontal component has a relatively larger error than the vertical

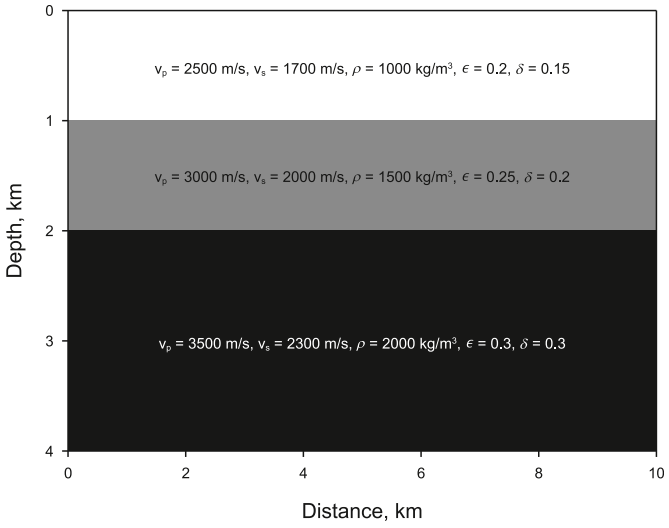

Fig. 9. The non-elliptical VTI layered model.

component. Besides, the variation in $\varepsilon - \delta$ has a slightly greater influence on the accuracy of wavefield separation than v_p/v_s. However, Fig. 8 indicates that even in strongly anisotropic media, e.g., $\varepsilon - \delta = 0.3$, the *RMSE* is about 2.3%. This suggests that the new method has a high level of accuracy and can be applied to most anisotropic media.

3.3. VTI layered model

In this example, we consider the VTI layered model, and the model parameters are shown in Fig. 9. The source is located at (5 km, 0.8 km) and is excited with a P-wave source of a 15-Hz Ricker wavelet. The grid spacing is 10 m in both horizontal and vertical directions.

The horizontal and vertical components of the particle velocity wavefields are shown in Fig. 10. The separated P and S waves are shown in Fig. 11. As can be seen, the leakage is weak. This implies that the proposed method is suitable for the VTI layered model.

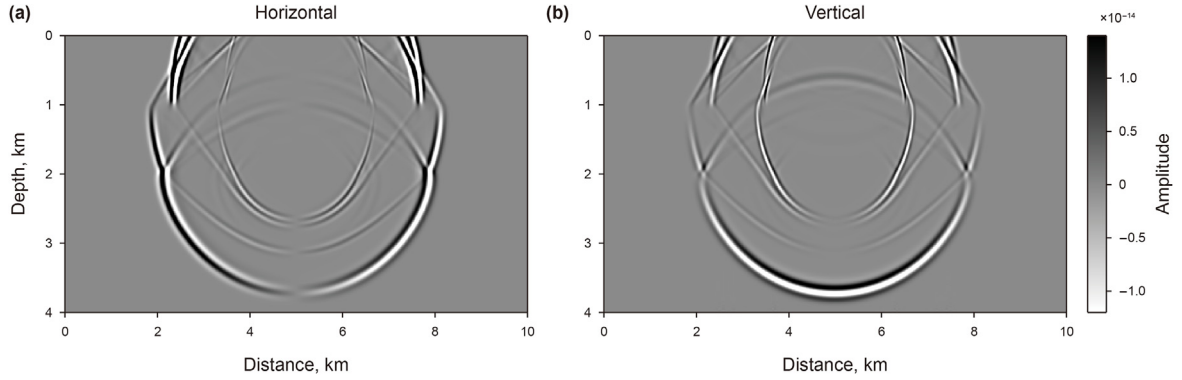

Fig. 10. The horizontal (**a**) and vertical (**b**) components of particle velocity for the non-elliptical VTI layer model.

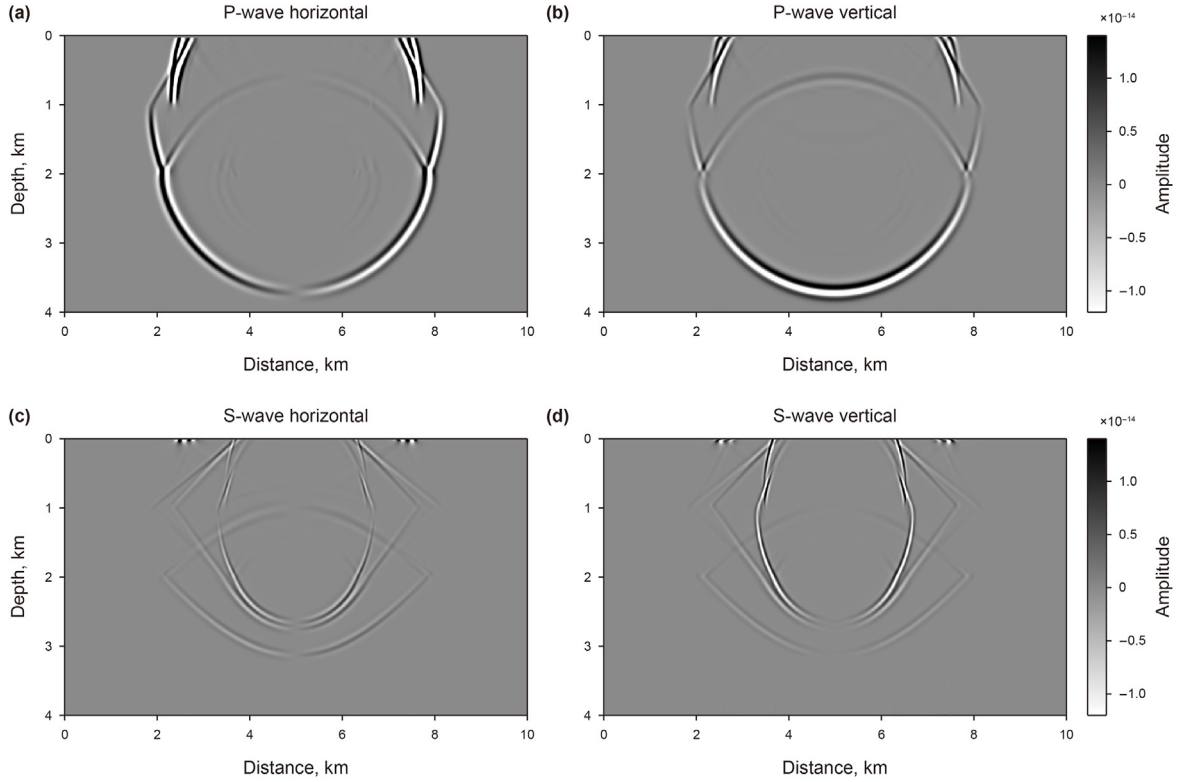

Fig. 11. The separated wavefields for the non-elliptical VTI layer model. Horizontal (**a**) and vertical (**b**) components of P-wave. Horizontal (**c**) and vertical (**d**) components of S-wave.

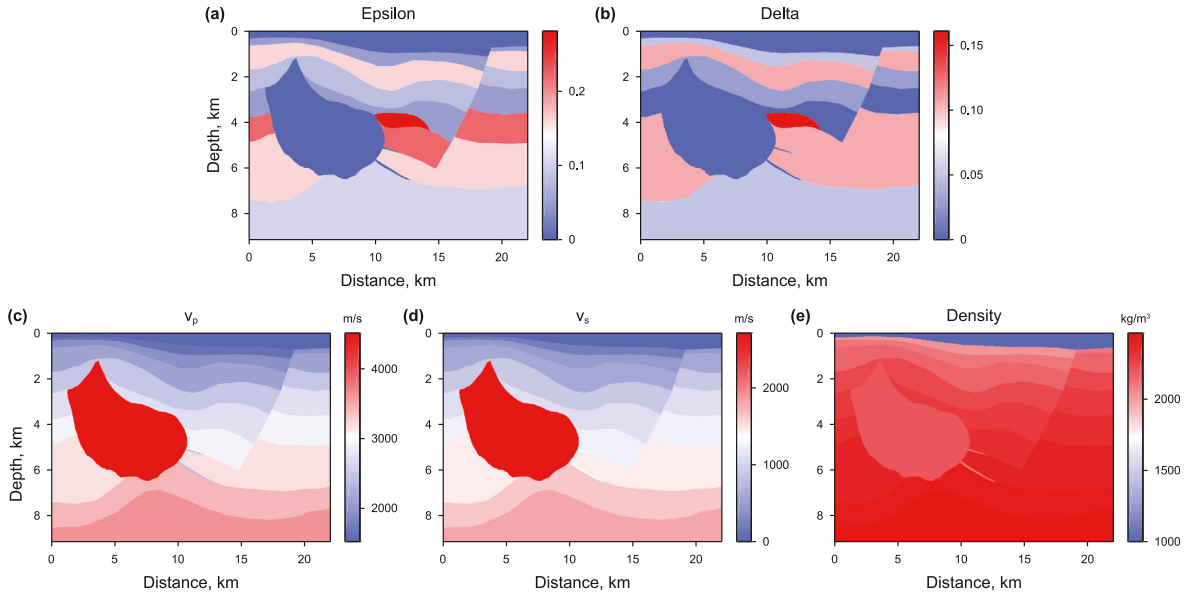

Fig. 12. Hess model parameters.

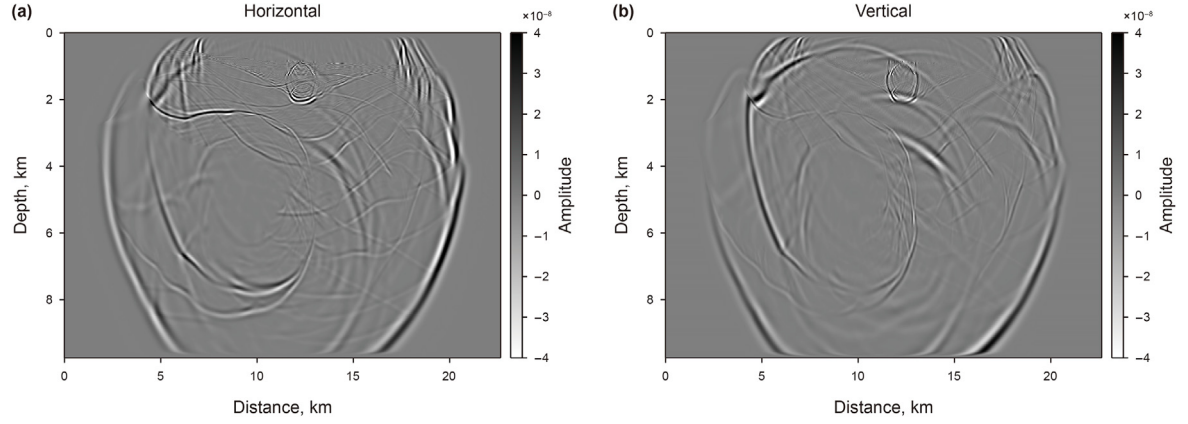

Fig. 13. The horizontal **(a)** and vertical **(b)** components of particle velocity wavefields in the Hess model.

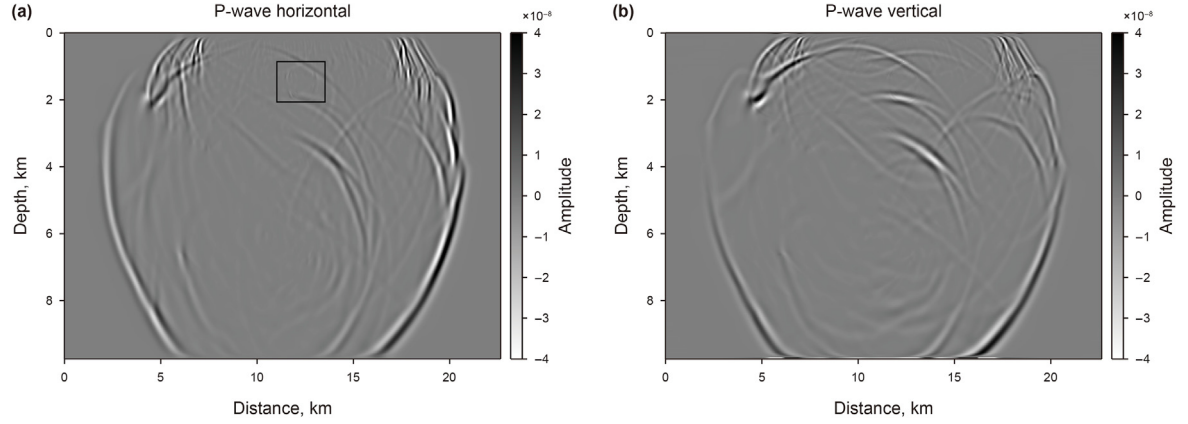

Fig. 14. The horizontal **(a)** and vertical **(b)** components of P-wave using the method of Yang et al. (2019).

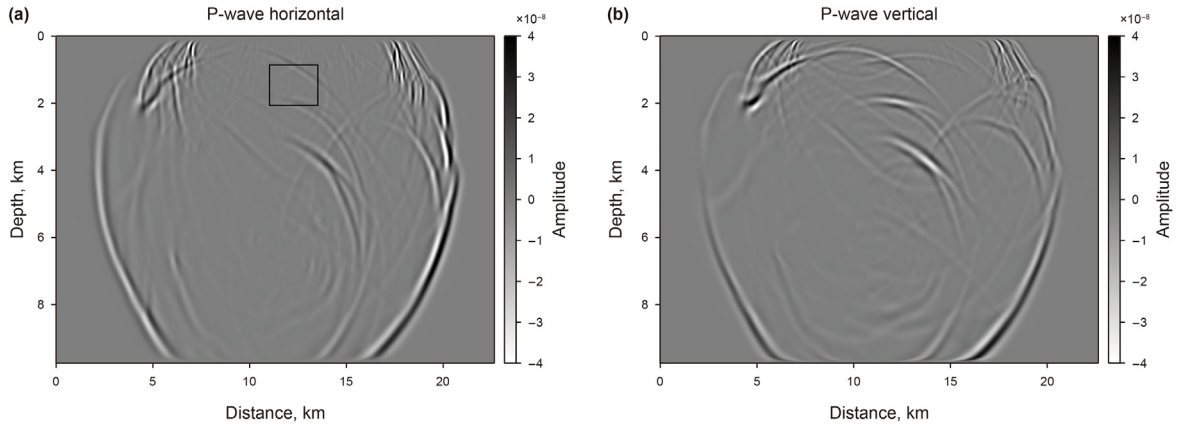

Fig. 15. The horizontal **(a)** and vertical **(b)** components of P-wave by using our method.

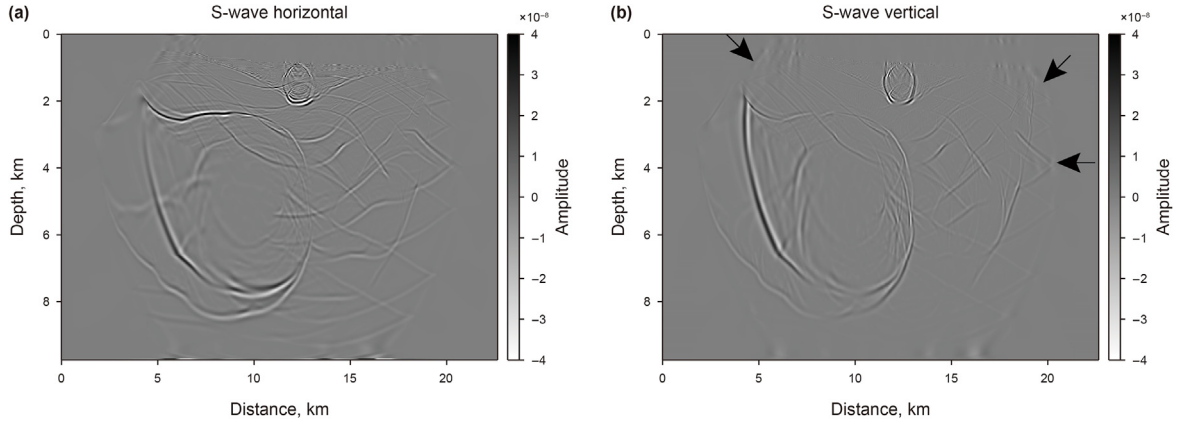

Fig. 16. The horizontal **(a)** and vertical **(b)** components of S-wave by using the method of Yang et al. (2019).

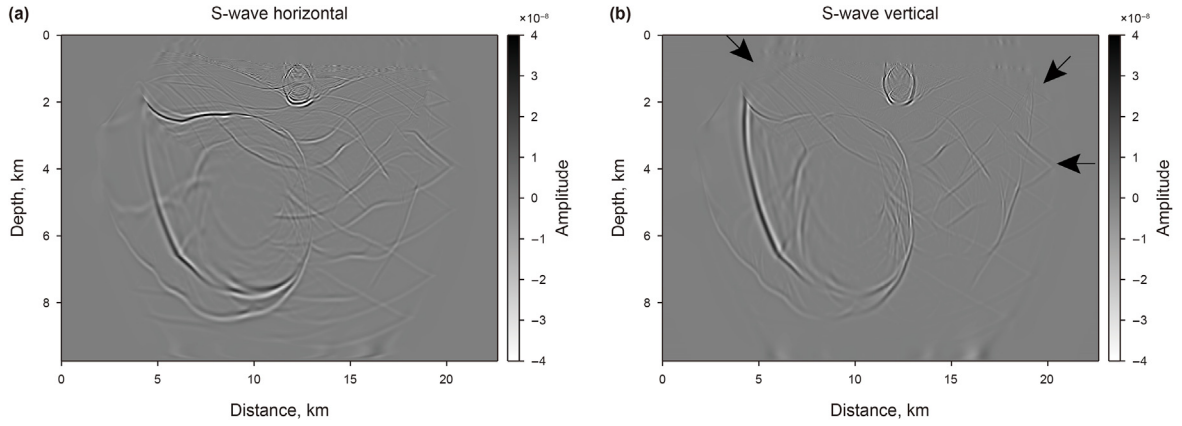

Fig. 17. The horizontal **(a)** and vertical **(b)** components of S-wave by using our method.

3.4. Hess model

The Hess model is further used to show the effectiveness of the proposed method in heterogeneous media. The model has a grid of 2205 × 915. The grid interval is 10 m. A 5-Hz Ricker wavelet is used as the vertical body-force source excitation. The source is placed at (12 km, 0.5 km). The input wavefield contains an absorbing boundary area. The model parameters are shown in Fig. 12(a)–(e).

Fig. 13 shows the horizontal and vertical components of particle velocity wavefields obtained through simulation. As a comparison, we first use the method of Yang et al. (2019) to separate P/S-waves. The results are shown in Fig. 14(a) and (b). As can be seen from Fig. 14(a), there is a faint S-wave residual indicated by the black box in the extracted P-wave. The S-wave residual almost cannot be seen

Table 1
The CPU times of the proposed method and that of Yang et al. (2019).

Model	Time cost of Yang's method	Time cost of the proposed method
Homogeneous model	6.22 s	3.13 s
Layered model	6.61 s	3.41 s
Hess model	43.05 s	21.82 s

in the extracted P-wave obtained by the method we proposed (Fig. 15(a)).

Figs. 16 and 17 show the separation results for S-wave. As can be seen, there are P-wave residuals in both S-waves, but Fig. 16(b) has more remnants than Fig. 17(b), which are indicated by the black arrows. The reason why a tiny amount of P-waves remains in S-waves in Figs. 16 and 17 is that these two methods are based on zero-order Taylor expansion to the exact eigenvalues, and therefore the resulting polarization direction is accurate when $\varepsilon = \delta$, and is an approximation when $\varepsilon \neq \delta$. But, in general, the pseudo-Helmholtz decomposition based on zero-order Taylor expansion achieves good wave separation for the Hess model, which is a representative model of the real world. In addition, previous studies have shown that the wavefield separation results obtained by using zero-order Taylor expansion can meet the needs of elastic migration imaging (Yang et al., 2019; Zhang et al., 2022; Zuo et al., 2022). The reason why our method is slightly better than Yang et al. (2019) is that, for 2D problems, Yang's method requires solving two anisotropic Poisson equations when computing the auxiliary vector wavefield, and requires a pseudo-divergence and a pseudo-gradient to obtain the P-wave. In addition, Yang's method requires two pseudo-curl operators to compute the S-wave. Errors will occur when using pseudo-gradient, pseudo-divergence, and pseudo-curl operators for approximating the corresponding exact operators. However, our algorithm only uses one anisotropic Poisson equation to compute the scalar auxiliary function and uses a pseudo-gradient operator to obtain the P-wave. Another reason is that the pseudo-derivative operator proposed by Yang et al. (2019) does not reduce into a derivative operator when the anisotropic parameters are zero. This tends to cause more errors.

To further show the efficiency of the proposed method, we compare the CPU time of the new method with that of Yang et al. (2019) for the homogeneous elliptical anisotropy model, the layered model, and the Hess model in the previous numerical examples. The running time is shown in Table 1. As can be seen, the computational cost of the proposed method is about 1/2 of that of Yang et al. (2019) for 2D problems.

4. Discussion

Zheng and Yao (2023) used the relationships between the gradient, divergence, curl, and exterior derivative operators to construct the isotropic scalar Poisson equation. In this paper, the anisotropic scalar Poisson equation was derived by constructing the pseudo-divergence, pseudo-gradient, and pseudo-curl operators through the polarization directions of P and S waves. The scalar anisotropic Poisson equation is an extension of the scalar isotropic Poisson equation. When the anisotropic parameter is zero, the pseudo-divergence, pseudo-gradient, and pseudo-curl operators reduce to the divergence, gradient, and curl operators in the isotropic media. In this case, the scalar anisotropic Laplace operator reduces to the scalar isotropic Laplace operator.

The scalar isotropic Poisson equation can be solved in the wavenumber domain, but the coefficients of the anisotropic Poisson equation vary in space, so the equation cannot be solved in the wavenumber domain directly by using FFT. In this paper, we propose to solve the scalar anisotropic Poisson equation in the spatial domain by using SOR iteration with alternating sweeping orderings. Eq. (19) is used to compute the scalar auxiliary function f without the need to construct a large coefficient matrix, which can significantly reduce the computational cost, as well as implementation complexity, compared with the matrix-based methods, e.g., LU decomposition. In our numerical experiment, the SOR method takes 15 iterations for the homogeneous media. For a more complex model, we can increase the iteration numbers for a more accurate solution of the function f, for instance, 60 iterations are used for the Hess model study.

5. Conclusion

In this paper, a new scalar anisotropic Poisson equation for pseudo-Helmholtz decomposition is proposed using pseudo-divergence, pseudo-gradient, and pseudo-curl operators. The vector P and S waves are decomposed by solving the scalar anisotropic Poisson equation. Thus, compared with the existing approaches based on solving the vector anisotropic Poisson equation, the proposed method saves the computational cost by half for 2D problems, respectively. The resulting separated P and S waves keep the correct amplitude and phase. The numerical experiments demonstrate the effectiveness of the methods we proposed. Especially, the Hess model shows that the pseudo-Helmholtz decomposition based zero-order Taylor expansion can achieve an effective wave separation, which can basically meet the needs of reverse-time migration imaging. This proposed method can be extended to 3D problems straightforwardly, which saves 2/3 of the cost.

Declaration of competing interest

The authors declare that they have no known competing financial interests or personal relationships that could have appeared to influence the work reported in this paper.

Acknowledgments

This work was supported by the National Key R&D Program of China (No. 2018YFA0702505), the project of CNOOC Limited (Grant No. CNOOC-KJ GJHXJSGG YF 2022-01), R&D Department of China National Petroleum Corporation (Investigations on fundamental experiments and advanced theoretical methods in geophysical prospecting application, 2022DQ0604-02), NSFC (Grant Nos. U23B20159, 41974142, 42074129, 12001311). We are grateful to the two anonymous reviewers, who gave valuable suggestions.

Appendix A

Wavefield decomposition for 3D anisotropic media using scalar anisotropic Poisson operators.

The elastic wave equation in the 3D VTI media is as follows:

$$\begin{cases} \rho\dfrac{\partial^2 u_x}{\partial t^2} = \left(c_{11}\dfrac{\partial^2}{\partial x^2} + c_{66}\dfrac{\partial^2}{\partial y^2} + c_{44}\dfrac{\partial^2}{\partial z^2}\right)u_x + (c_{11}-c_{66})\dfrac{\partial^2 u_y}{\partial x\partial y} + (c_{13}+c_{44})\dfrac{\partial^2 u_z}{\partial x\partial z} \\ \rho\dfrac{\partial^2 u_y}{\partial t^2} = (c_{11}-c_{66})\dfrac{\partial^2 u_x}{\partial x\partial y} + \left(c_{66}\dfrac{\partial^2}{\partial x^2} + c_{11}\dfrac{\partial^2}{\partial y^2} + c_{44}\dfrac{\partial^2}{\partial z^2}\right)u_y + (c_{13}+c_{44})\dfrac{\partial^2 u_z}{\partial y\partial z} \\ \rho\dfrac{\partial^2 u_z}{\partial t^2} = (c_{13}+c_{44})\dfrac{\partial^2 u_x}{\partial x\partial z} + (c_{13}+c_{44})\dfrac{\partial^2 u_y}{\partial y\partial z} + \left(c_{44}\dfrac{\partial^2}{\partial x^2} + c_{44}\dfrac{\partial^2}{\partial y^2} + c_{33}\dfrac{\partial^2}{\partial z^2}\right)u_z \end{cases} \tag{A.1}$$

where u_x,u_y,u_z are two horizontal and one vertical components of the displacements in Cartesian coordinates, respectively. They are functions of time and space. c_{11}, c_{13}, c_{33}, c_{44} and c_{66} are the elements of the elastic coefficient matrix, and ρ represents density. They are functions of space. Under the assumption of local homogeneity, the elastic coefficient matrix elements can be represented by Thomsen parameters (Thomsen, 1986):

$$\begin{aligned} &c_{11} = \rho(1+2\varepsilon)v_{\mathrm{p}}^2, c_{33} = \rho v_{\mathrm{p}}^2 \\ &c_{44} = c_{55} = \rho v_{\mathrm{s}}^2, c_{66} = \rho(1+2\gamma)v_{\mathrm{s}}^2 \\ &c_{13} = \rho\sqrt{\left[(1+2\delta)v_{\mathrm{p}}^2 - v_{\mathrm{s}}^2\right]\left[v_{\mathrm{p}}^2 - v_{\mathrm{s}}^2\right]} - \rho v_{\mathrm{s}}^2 \end{aligned} \tag{A.2}$$

where ε, δ and γ are the Thomsen anisotropy parameters, v_{p} and v_{s} denote the P-wave and S-wave velocities along the axis of symmetry, respectively.

Like the 2D media, the polarization directions of the P and S waves can be obtained by using the Christoffel equation. See Zuo et al. (2022) for more details. For a 3D problem, we can define the pseudo-gradient operator with the polarization direction of the P-wave by

$$\tilde{\nabla} = \begin{bmatrix} \partial_x \\ \partial_y \\ r(\mathbf{x})\partial_z \end{bmatrix} \tag{A.3}$$

where $r(\mathbf{x})$ is defined in Eq. (8). Then, the P- and S-wavefield decomposition equations for 3D anisotropic media are

$$\mathbf{u}^{\mathrm{p}} = \tilde{\nabla} f,\ \mathbf{u}^{\mathrm{s}} = \mathbf{u} - \mathbf{u}^{\mathrm{p}} \tag{A.4}$$

Here the scalar auxiliary function f satisfies the following anisotropic Poisson equation:

$$\frac{\partial^2 f(\mathbf{x})}{\partial x^2} + \frac{\partial^2 f(\mathbf{x})}{\partial y^2} + r^2(\mathbf{x})\frac{\partial^2 f(\mathbf{x})}{\partial z^2} = \tilde{\nabla}\cdot\mathbf{u}(\mathbf{x}) \tag{A.5}$$

By denoting

$$b(\mathbf{x}) = r^2(\mathbf{x}), w(\mathbf{x}) = \tilde{\nabla}\cdot\mathbf{u}(\mathbf{x}) \tag{A.6}$$

Eq. (A.5) then can be expressed as

$$\frac{\partial^2 f(\mathbf{x})}{\partial x^2} + \frac{\partial^2 f(\mathbf{x})}{\partial y^2} + b(\mathbf{x})\frac{\partial^2 f(\mathbf{x})}{\partial z^2} = w(\mathbf{x}) \tag{A.7}$$

Similarly, the 3D anisotropic Poisson equation (Eq. (A.7)) can also be solved using SOR iterative with alternating sweeping orderings. When $i = 1{:}I, \mathrm{l} = 1:\mathrm{L}, j = 1{:}J$, SOR iteration format is as follows, and iteration formats under other sequential iterations can also be analogized:

$$f_{i,l,j}^{(k+1)} = \frac{\beta}{c_0\left(\frac{1}{\Delta x^2}+\frac{1}{\Delta y^2}+\frac{b_{i,l,j}}{\Delta z^2}\right)}\begin{pmatrix} w_{i,l,j} - \dfrac{1}{\Delta x^2}\displaystyle\sum_{n=1}^{3} c_n\left(f_{i+n,l,j}^{(k)} + f_{i-n,l,j}^{(k+1)}\right) \\ -\dfrac{1}{\Delta y^2}\displaystyle\sum_{n=1}^{3} c_n\left(f_{i,l+n,j}^{(k)} + f_{i,l-n,j}^{(k+1)}\right) \\ -\dfrac{b_{i,l,j}}{\Delta z^2}\displaystyle\sum_{n=1}^{3} c_n\left(f_{i,l,j+n}^{(k)} + f_{i,l,j-n}^{(k+1)}\right) \end{pmatrix} + (1-\beta)f_{i,l,j}^{(k)} \tag{A.8}$$

Based on Eqs. (A.1)–(A.8), the wavefield decomposition method based on the proposed scalar anisotropic Poisson equation for 3D VTI media is briefly discussed in this section. The existing 3D anisotropic wavefield decomposition method proposed by Zuo et al. (2022) requires solving the anisotropic Poisson equation three times, whereas our method only requires solving it once. In theory, our method can potentially reduce the computational workload by 2/3 compared to the existing approaches.

References

Aki, K., Richards, P.G., 2002. Quantitative Seismology. University Science Books, California.

Cheng, J.B., Fomel, S., 2014. Fast algorithms for elastic-wave-mode separation and vector decomposition using low-rank approximation for anisotropic media. Geophysics 79 (4), C97–C110. https://doi.org/10.1190/geo2014-0032.1.

Dellinger, J., Etgen, J., 1990. Wave-field separation in two-dimensional anisotropic media. Geophysics 55 (7), 914–919. https://doi.org/10.1190/1.1442906.

Dellinger, J.A., 1991. Anisotropic Seismic Wave Propagation. Stanford University.

Du, Q.Z., Guo, C.F., Zhao, Q., et al., 2017. Vector-based elastic reverse time migration based on scalar imaging condition. Geophysics 82 (2), S111–S127. https://doi.org/10.1190/geo2016-0146.1.

Hu, Y., Pan, Y.D., Xia, J.H., 2022. Wavefield-separated full-waveform inversion of shallow-seismic Rayleigh waves. Pure Appl. Geophys. 179 (5), 1583–1596. https://doi.org/10.1007/s00024-022-02995-0.

Kincaid, D.R., Young, D.M., 1972. The modified successive overrelaxation method with fixed parameters. Math. Comput. 26 (119), 705–717. https://doi.org/10.1090/S0025-5718-1972-0331746-2.

Li, Z.Y., Liu, Y.S., Liang, G.H., et al., 2021. First-order particle velocity equations of decoupled P- and S-wavefields and their application in elastic reverse time migration. Geophysics 86 (6), S387–S404. https://doi.org/10.1190/geo2020-0452.1.

Li, Z.C., Qu, Y.M., 2022. Research progress on seismic imaging technology. Petrol. Sci. 19 (1), 128–146. https://doi.org/10.1016/j.petsci.2022.01.015.

Lu, Y.M., Liu, Q.C., Zhang, J.F., et al., 2019. Poynting and polarization vectors based wavefield decomposition and their application on elastic reverse time migration in 2D transversely isotropic media. Geophys. Prospect. 67 (5), 1296–1311. https://doi.org/10.1111/1365-2478.12777.

Luo, J.R., Wang, B.F., Wu, R.S., et al., 2020. Elastic full waveform inversion with angle decomposition and wavefield decoupling. IEEE Trans. Geosci. Rem. Sens. 59 (1),

871–883. https://doi.org/10.1109/TGRS.2020.2994959.
Morse, P.M., Feshbach, H., 1953. Methods of Theoretical Physics. McGraw-Hill Book Company.
Qu, Y.M., Li, J.L., Li, Z.C., et al., 2018. An elastic full-waveform inversion based on wave-mode separation. Explor. Geophys. 49 (4), 530–552. https://doi.org/10.1071/EG16158.
Ren, Z.M., Liu, Y., 2016. A hierarchical elastic full-waveform inversion scheme based on wavefield separation and the multistep-length approach. Geophysics 81 (3), R99–R123. https://doi.org/10.1190/geo2015-0431.1.
Sripanich, Y., Fomel, S., Sun, J.Z., et al., 2017. Elastic wave-vector decomposition in heterogeneous anisotropic media. Geophys. Prospect. 65 (5), 1231–1245. https://doi.org/10.1111/1365-2478.12482.
Sun, R., McMechan, G.A., Hsiao, H.H., et al., 2004. Separating P- and S-waves in prestack 3D elastic seismograms using divergence and curl. Geophysics 69 (1), 286–297. https://doi.org/10.1190/1.1649396.
Sun, R., McMechan, G.A., Lee, C.S., et al., 2006. Prestack scalar reverse-time depth migration of 3D elastic seismic data. Geophysics 71 (5), S199–S207. https://doi.org/10.1190/1.2227519.
Thomsen, L., 1986. Weak elastic anisotropy. Geophysics 51 (10), 1954–1966. https://doi.org/10.1190/1.1442051.
Xie, C., Song, P., Li, X.S., et al., 2021. Angle-weighted reverse time migration with wavefield decomposition based on the optical flow vector. Front. Earth Sci. 9, 732123. https://doi.org/10.3389/feart.2021.732123.
Yan, J., Sava, P., 2008. Isotropic angle-domain elastic reverse-time migration. Geophysics 73 (6), S229–S239. https://doi.org/10.1190/1.2981241.
Yan, J., Sava, P., 2009. Elastic wave-mode separation for VTI media. Geophysics 74 (5), WB19–WB32. https://doi.org/10.1190/1.3184014.
Yang, J.D., Zhu, H.J., Wang, W.L., et al., 2018. Isotropic elastic reverse time migration using the phase- and amplitude-corrected vector P- and S-wavefields. Geophysics 83 (6), S489–S503. https://doi.org/10.1190/geo2018-0023.1.
Yang, J.D., Zhang, H.Z., Zhao, Y., et al., 2019. Elastic wavefield separation in anisotropic media based on eigenform analysis and its application in reverse-time migration. Geophys. J. Int. 217 (2), 1290–1313. https://doi.org/10.1093/gji/ggz085.
Zhang, L.L., Liu, L., Niu, F.L., et al., 2022. A novel and efficient engine for P-/S-wave-mode vector decomposition for vertical transverse isotropic elastic reverse time migration. Geophysics 87 (4), S185–S207. https://doi.org/10.1190/geo2021-0609.1.
Zhang, L.L., Zhao, Y., Liu, L., et al., 2023. A fast anisotropic decoupled operator of elastic wave propagation in the space domain for P/S wave-mode decomposition and angle calculation, with its application to elastic reverse time migration in TI medium. Geophysics 88 (3), T151–T164. https://doi.org/10.1190/geo2022-0477.1.
Zhang, Q.S., McMechan, G.A., 2010. 2D and 3D elastic wavefield vector decomposition in the wavenumber domain for VTI media. Geophysics 75 (3), D13–D26. https://doi.org/10.1190/1.3431045.
Zhang, W., Shi, Y., 2019. Imaging conditions for elastic reverse time migration. Geophysics 84 (2), S95–S111. https://doi.org/10.1190/geo2018-0197.1.
Zhao, H., 2005. A fast sweeping method for eikonal equations. Math. Comput. 74 (250), 603–627. https://doi.org/10.1090/S0025-5718-04-01678-3.
Zhao, Y., Zhang, H.Z., Yang, J.D., et al., 2018. Reducing artifacts of elastic reverse time migration by the deprimary technique Deprimary ERTM. Geophysics 83 (6), S569–S577. https://doi.org/10.1190/geo2018-0260.1.
Zheng, Q.Q., Yao, G., 2023. An improved elastic wavefield separation method based on the Helmholtz decomposition. Geophysics 88 (4), T203–T210. https://doi.org/10.1190/geo2022-0628.1.
Zhong, Y., Gu, H.M., Liu, Y.T., et al., 2021. Elastic reverse-time migration with complex topography. Energies 14 (23), 7837. https://doi.org/10.3390/en14237837.
Zhou, X.Y., Chang, X., Wang, Y.B., et al., 2019. Amplitude-preserving scalar PP and PS imaging condition for elastic reverse time migration based on a wavefield decoupling method. Geophysics 84 (3), S113–S125. https://doi.org/10.1190/geo2017-0840.1.
Zhou, Y., Wang, H.Z., 2017. Efficient wave-mode separation in vertical transversely isotropic media. Geophysics 82 (2), C35–C47. https://doi.org/10.1190/geo2016-0191.1.
Zhu, H.J., 2017. Elastic wavefield separation based on the Helmholtz decomposition. Geophysics 82 (2), S173–S183. https://doi.org/10.1190/geo2016-0419.1.
Zuo, J.H., Niu, F.L., Liu, L., et al., 2022. 3D anisotropic P- and S-mode wavefields separation in 3D elastic reverse-time migration. Surv. Geophys. 43 (3), 673–701. https://doi.org/10.1007/s10712-021-09688-8.